Published in : Journal of Energy Chemistry (2022), vol. 65, pp. 210–218
DOI: 10.1016/j.jechem.2021.05.050
Status : Postprint (Author's version)

HIGH TEMPERATURE X-RAY DIFFRACTION STUDY OF THE FORMATION OF $Na_2Ti_3O_7$ FROM A MIXTURE OF SODIUM CARBONATE AND TITANIUM OXIDE

Caroline Piffet[a], Bénédicte Vertruyen[a], Frédéric Hatert[b], Rudi Cloots[a], Frédéric Boschini[a], Abdelfattah Mahmoud[a]

[a] *GREENMAT, CESAM Research Unit, Chemistry Department, University of Liège, 4000 Liège, Belgium*
[b] *Laboratory of Mineralogy, Geology Research Unit, University of Liège, 4000 Liège, Belgium*

Abstract

$Na_2Ti_3O_7$ has attracted much attention in the field of anode materials for Na-ion batteries thanks to its non-toxicity and very low working potential of 0.3V vs Na^0/Na^+. Building a clearer picture of its formation from cheap Na_2CO_3 and TiO_2 starting materials is therefore of obvious interest. Here, we report new insights from an in-situ high temperature X-ray diffraction study conducted from room temperature to 800°C, complemented by ex-situ characterizations. We were thereby able to position the previously reported $Na_4Ti_5O_{12}$ and $Na_2Ti_6O_{13}$ intermediate phases in a reaction scheme involving three successive steps and temperature ranges. Shifts and/or broadening of a subset of the $Na_2Ti_6O_{13}$ reflections suggested a combination of intra-layer disorder with the well-established ordering of successive layers. This in-situ study was carried out on reproducible mixtures of Na_2CO_3 and TiO_2 in 1:3 molar ratio prepared by spray-drying of mixed aqueous suspensions. Single-phase $Na_2Ti_3O_7$ was obtained after only 8h at 800°C in air, instead of a minimum of 20h for a conventional solid-state route using the same precursors. Microstructure analysis revealed ~15µm diameter granules made up from rectangular rods of a few-µm length presenting electrochemical properties in line with expectations. In the absence of grinding or formation of intimate composites with conductive carbon, the specific capacity of 137 mAh/g at C/5 decreased at higher rates.

Keywords: Formation mechanism, High temperature XRD, $Na_2Ti_3O_7$, Spray-drying synthesis, Na-ion batteries

1. INTRODUCTION

In order to meet the challenges of building a more sustainable world, fossil fuels are progressively being replaced by renewable and green energy sources such as wind, sun, water, etc. Because of the intermittent character of such sources, efficient energy storage systems are necessary. Since the nineties, lithium-ion batteries (LIBs) have become one of the dominant technologies in this domain. However, the inhomogeneous localization and the questions surrounding the availability of lithium resources mean that Na-ion batteries (NIBs) are obvious candidates for large-scale and energy grid storage [1–5]. Indeed, sodium is an abundant element (the 4th most abundant element in the Earth's crust with an abundance of around 2.8% [5]) with widespread distribution. Hard carbon materials are currently the most common active anode materials for NIBs [6], but non carbonaceous alternatives are also under investigation for cases where thermal stability is prioritized [7]. Amongst the transition

Published in : Journal of Energy Chemistry (2022), vol. 65, pp. 210–218
DOI: 10.1016/j.jechem.2021.05.050
Status : Postprint (Author's version)

metals, titanium is non-toxic, low-cost and abundant (the second most abundant transition metal after iron [5]). Sodium titanates are therefore studied as anode materials for NIBs [8,9], with $Na_2Ti_3O_7$ (NTO) being one of the most appealing sodium titanate anode candidates thanks to its insertion potential of 0.3V vs Na^0/Na^+, which is one of the lowest reported working potentials for NIB anode insertion-type materials [10]. During the electrochemical processes, 2/3 of the titanium atoms are reduced/oxidized from Ti^{4+} to Ti^{3+}/ from Ti^{3+} to Ti^{4+} while two Na^+ ions insert/extract in its structure: $Na_2Ti_3O_7 + 2Na^+ + 2e^- \leftrightarrow Na_4Ti_3O_7$, which corresponds to a theoretical capacity of 178 mAh/g [10,11].

Some information about the sequence of intermediate phases during the formation of $Na_2Ti_3O_7$ have already been reported in the literature for hydrothermal [12,13], sol–gel [14] or solid-state [15–17] synthesis routes, sometimes as part of studies where $Na_2Ti_3O_7$ is under consideration for use in other applications such as gas sensors, photocatalysts and ion exchangers [18,19]. These studies rely on diffractograms collected ex-situ after heat treatments at a few different temperatures, while a better understanding of the formation mechanism would benefit from the clearer view offered by in-situ high temperature X-ray diffraction. This is especially true for the solid-state reaction of mixtures of TiO_2 and Na_2CO_3, which is a cheaper option for large-scale production than the hydrothermal and sol–gel routes involving titanium alkoxides as a titanium precursor [12–14]. For the preparation of large batches, homogenization of the mixture of TiO_2 and Na_2CO_3 by spray-drying a suspension is an easy, reproducible and largescale production method [20–22], with the possibility of easily adding carbon into the mix [23] and better control the microstructural properties. It is actually also possible to dry sol–gel precursors, as shown for example in the work of Zou et al. [24,25] where a precursor of $Na_2Ti_3O_7$ was prepared by spray-drying starting from tetrabutyl titanate (TBT) and sodium acetate in a mixture of solvents). The spray drying technique has thus great interest in the development of electrode materials for secondary batteries [23].

Here we report on an in-situ high temperature X-ray diffraction study conducted during the heat treatment of a precursor prepared by spray-drying a dispersion of TiO_2 and Na_2CO_3 in water. By combining this in-situ study with a range of ex-situ characterizations, we propose a detailed mechanism in three steps for the formation of $Na_2Ti_3O_7$. Microstructural and electrochemical data are also reported to complement the detailed structural information and provide a comprehensive description of the material.

2. MATERIALS AND METHODS

2.1. MATERIALS

Nano-TiO_2 (Aeroxide P25, 99.5%+, Evonik), Duramax D-3005 (ammonium salt of a polyelectrolyte, kindly provided by Dow Chemical), Na_2CO_3 (anhydrous 99.0%+, Sigma Aldrich), carbon black (CB, Alpha Aesar, 50% compressed, 99.9%+), multiwall carbon nanotubes (CNT, 5 wt% dispersion ORGACYL™ NMP0502, Nanocyl), N-methyl-2-pyrrolidone (NMP, 99.5%, Sigma Aldrich), polyvinylidene fluoride (PVDF, Sigma Aldrich), $NaClO_4$ (≥98.0%, Sigma Aldrich), propylene carbonate (PC, 99.7%, Sigma Aldrich) and ethylene carbonate (EC, 99.0% Sigma Aldrich) were used as received.

Published in : Journal of Energy Chemistry (2022), vol. 65, pp. 210–218
DOI: 10.1016/j.jechem.2021.05.050
Status : Postprint (Author's version)

2.2. SPRAY-DRYING SYNTHESIS

In a typical experiment, a 10 wt% TiO_2 aqueous suspension was prepared by dispersing nano-TiO_2 (10–50 nm, with a major particle size distribution of 15–25nm [26]) in water with Duramax D-3005 (3 wt% with respect to TiO_2). Na_2CO_3 was then added in stoichiometric ratio (Na:Ti = 2:3) under stirring. The slurry was injected in air using a rotary injector into a Niro Mobile Minor spraydryer. The inlet temperature was set at 190°C to target an outlet temperature of 110–120°C. The flow rate was set at 25 mL/min and the air pressure at 3 bars. The spray-dried powders were then heat-treated in air at different temperatures with a heating rate of 2°C/min.

2.3. CHARACTERIZATIONS

The morphology and size of the particles were examined using scanning electron microscopy (ESEM XL-30, FEI) and transmission electron microscopy (Tecnai G2 TWIN, FEI). Samples for SEM were prepared by placing the powders on carbon tapes, followed by gold coating. A cross-section sample was obtained by dispersing the powder in an epoxy resin and polishing followed by gold coating. Samples for TEM were prepared by dispersing the powders by ball-milling in isopropanol (about 150mg of powder for 2g of solvent), using miller Retsch PM400/2, zirconia balls with a diameter of 1.5mm). 2–3 drops of that dispersion was then poured on TEM grid and sample dried at ambient temperature. The particle size distribution was measured by laser diffraction granulometry (Malvern Mastersizer 2000 Hydro). The BET specific surface area was determined from N_2 sorption isotherms measured at 77 K for relative pressure P/P^0 between 0 and 0.3 with a Micromeritics Asap 2020 Plus instrument. Degassing was applied for 180 min at 150°C with a heating ramp of 10°C/min. The Rouquerol criteria were used to select the pressure range used to estimate the BET surface [27]. X-ray diffraction (XRD) patterns were collected with a Bruker D8 Twin-Twin diffractometer (Cu Kalpha radiation). In-situ XRD analysis was performed with a high temperature HTK1200 chamber (see photographs in Fig. S1) in air atmosphere with a heating rate of 2°C/ min. Quantification of the crystalline phases was performed by Rietveld refinements of the scale factors in the TOPAS software using the fundamental parameters approach to model the instrumental contribution. The structural models were taken from the PDF4+ database for TiO_2 anatase (00–021-1272), TiO_2 rutile (00– 021-1276), Na_2CO_3 (01–075-6816) $Na_2Ti_3O_7$ (04–015-7486), $Na_2Ti_6O_{13}$ (01–080-5525) and $Na_4Ti_5O_{12}$ (00–052-1814). Thermogravimetric curves and differential scanning calorimetry were collected on a TA instrument in air from 40 to 900°C with a heating rate of 2°C/min. Electrochemical measurements were carried out in coin cell configuration (2032). Working electrodes were prepared by dispersing 70 wt% NTO with 20 wt% carbon as a conductive additive and 10 wt% PVDF as a binder in NMP solvent. The carbon source was a CB:CNT mixture in 1:3 weight ratio because CNTs are known to lead to a better capacity retention and rate capability [28,29]. The slurry was tape-casted (Byko-drive XL, BYK) on copper foil and dried at 110°C for 12h under vacuum. Metallic Na was used as a reference and a counter electrode. The electrolyte was a 1 M $NaClO_4$ solution in PC:EC (1:1 v:v) solvent, as commonly used for electrochemical measurements on $Na_2Ti_3O_7$ [30]. Watman glass fiber was used as a separator. Electrochemical measurements were performed with a multichannel BTS Neware Potentiostat (cycling) or a multichannel BioLogic VMP3 potentiostat/galvanostat (cyclic voltammetry), in a voltage window of 0.05–1.5V vs Na^0/Na^+.

Published in : Journal of Energy Chemistry (2022), vol. 65, pp. 210–218
DOI: 10.1016/j.jechem.2021.05.050
Status : Postprint (Author's version)

3. RESULTS AND DISCUSSIONS

3.1. PRECURSORS

The XRD pattern of the as-sprayed powder (Fig. 1a) displays the diffraction peaks corresponding to the expected mixture of Na_2CO_3, TiO_2 anatase and TiO_2 rutile. The Rietveld quantification of the crystalline phases (27 wt% Na_2CO_3, 63 wt% anatase and 10 wt% rutile) is in good agreement with the nominal values of 30 wt% Na_2CO_3 + 70 wt% TiO_2 and with the total mass loss of about 14.3 wt% in the thermogravimetric curve presented in Fig. 1b. This mass loss is accompanied by an endothermic signal in the differential scanning calorimetry curve, also shown in Fig. 1b. The global reaction to consider is $Na_2CO_3 + 3\ TiO_2 \rightarrow Na_2Ti_3O_7 + CO_2$, corresponding to a CO_2 release of 12.7 wt%, with the additional mass loss of 1.6 wt% attributed to the decomposition of the Duramax D-3005 dispersant and possibly some residual adsorbed water. A scanning electron micrograph shows spherical particles with a diameter of 3–30µm (Fig. 1c).

3.2. $Na_2Ti_3O_7$ FORMATION MECHANISM

The sequence of phases observed during the formation of $Na_2Ti_3O_7$ was studied by combining in-situ and ex-situ XRD and is described in this section.

The intensity maps in Fig. 2 (a-b) plot the intensity of the diffraction peaks as a function of the temperature from room temperature to 800°C. The complete set of in-situ high temperature XRD patterns above 500 C can be found in Fig. S2. Up to 523°C (Fig. 2a), only the reflections associated with Na_2CO_3 display significant changes: the peaks initially located at 30.2°2θ, 34.52θ, 35.2°2θ and 40°2θ shift in accordance with the evolution of cell parameters reported by P. Ballirano in his study of the polymorphism of Na_2CO_3 [31]. Starting at 524–538°C, a new small peak appears at 33.5°2θ, as shown in the selection of diffractograms in Fig. 2c. Its intensity increases and additional peaks become visible from 539-553°C. This set of reflections corresponds well to the $Na_4Ti_5O_{12}$ structure. TiO_2 (both anatase and rutile) are still present at this temperature. Then, no significant phenomenon occurs until 686–700°C (Fig. 2b), as confirmed by the plateaus in the plot of peak intensities vs temperature in Fig. 3. Starting at 686–700°C, the TiO_2 peaks disappear and the $Na_4Ti_5O_{12}$ peaks decrease while another titanate phase appears. The identification of this phase as $Na_2Ti_6O_{13}$ is discussed in more detail later (Fig. 4 and related text). The peak intensities of $Na_4Ti_5O_{12}$ and $Na_2Ti_6O_{13}$ reach a plateau (see Fig. 3) until the $Na_2Ti_3O_7$ phase emerges at 775–788°C and then develops at the expense of $Na_4Ti_5O_{12}$ and $Na_2Ti_6O_{13}$ when the sample is maintained at 800°C (Fig. 2(b;d) and Fig. 3). In summary, the in-situ high temperature XRD experiment confirms the formation of two intermediate titanate phases ($Na_4Ti_5O_{12}$ and $Na_2Ti_6O_{13}$) during the formation of $Na_2Ti_3O_7$ by solid-state reaction of Na_2CO_3 and TiO_2, as already observed by other authors in ex-situ experiments [32]. Traces of $Na_2Ti_6O_{13}$ were also found in $Na_2Ti_3O_7$ synthesized by solid-state reaction of TiO_2 with NaOH or CH_3COONa [15], while Zarrabeitia et al. [33] and Alava et al. [34] reported using an excess of the sodium salt for the solid-state synthesis of $Na_2Ti_3O_7$ in order to avoid the presence of residual $Na_2Ti_6O_{13}$ as a secondary phase.

Based on the evolution of the peak intensities in the in-situ diffraction data (Fig. 3), we can propose a process in three steps for the formation mechanism of $Na_2Ti_3O_7$ starting from a stoichiometric ratio of Na_2CO_3 and TiO_2:

$14\ Na_2CO_3 + 42\ TiO_2 \rightarrow 7\ Na_4Ti_5O_{12} + 7\ TiO_2 + 14\ CO_2$ (Step 1)

Published in : Journal of Energy Chemistry (2022), vol. 65, pp. 210–218
DOI: 10.1016/j.jechem.2021.05.050
Status : Postprint (Author's version)

$7\ Na_4Ti_5O_{12} + 7\ TiO_2 \rightarrow 6\ Na_4Ti_5O_{12} + 2\ Na_2Ti_6O_{13}$ (Step 2)

$6\ Na_4Ti_5O_{12} + 2\ Na_2Ti_6O_{13} \rightarrow 14\ Na_2Ti_3O_7$ (Step 3)

To corroborate this mechanism, the theoretical phase percentages based on the above equations should be compared to experimental quantification results. The data from the in-situ experiment were not appropriate for a Rietveld refinement of the phase percentages since they were collected in a limited 2θ range while the temperature was increasing. Therefore, several ex-situ diffractograms (Fig. S3) were collected on quenched samples taken out of a furnace when specific temperatures had been reached. Before proceeding with the Rietveld refinement of the phase percentages, it became necessary to take a closer look at the $Na_2Ti_6O_{13}$ phase because, both in the in-situ and the ex-situ diffractograms, the pattern of peaks did not correspond completely to the reported phase in PDF 01–080-5525 and references [35–39]. As shown in Fig. 4a, the sharp peaks corresponding to the (200), (110) and (310) reflections are found at the proper 2θ positions, indicating that the interplane distances d_{hkl} for these families of crystallographic planes are the same as in the reference $Na_2Ti_6O_{13}$ structure. As shown in Fig. 4b, these planes are parallel to the c axis and are associated with the periodicity of the layers of Na ions and edge-sharing TiO_6 in the structure. On the other hand, the (201) reflection is broadened towards higher d values (from d ~ 6.3 Å to d ~ 6.5 Å) and several reflections at higher 2θ angles are broadened and/or shifted. A possible explanation can be advanced based on the projection of the crystal structure along the b axis shown in Fig. 4c: whereas the thickness of the layers is constant, their local extension along c could vary slightly due to disorder and defects, possibly Na/Ti exchanges. We could not create a structural model for such a complex structure, therefore, only Step 1 is considered in Table 1 where the theoretical and experimental mass percentages are compared and found to be rather similar.

Table 1

Comparison of crystalline phase percentages in wt% obtained by Rietveld refinement of diffractograms collected on quenched samples (Rietveld columns) and values calculated based on the chemical equation of Step 1 (''calc." columns).

Sample	550 °C-0 h		650 °C-0 h		700 °C-0 h	
	Rietveld	Calc.	Rietveld	Calc.	Rietveld	Calc.
Na_2CO_3	32.0	30.7				
TiO_2 anatase + rutile	68.0	69.3	12.0	13.2	15.0	13.2
$Na_4Ti_5O_{12}$			88.0	86.8	85.0	86.8

Fig. 5 shows an overview of the reaction scheme corresponding to the equations of steps 1 to 3. The volume percentages of the different phases were calculated (see Table S1) and plotted in the colored diagram. The TEM micrographs a-f were collected on samples taken out of a furnace at different stages of the synthesis (see Fig. S3 for the ex-situ X-ray diffractograms) and illustrate the evolution of the microstructure. It is easy to identify the small TiO_2 particles (typically 20 nm) in micrographs a and b (before and during Step 1). Between Step 1 and Step 2 (micrographs c and d), TiO_2 particles are still visible as a minor component, in agreement with the calculated volume percentages, while the $Na_4Ti_5O_{12}$ phase forms larger particles. During Step 2, $Na_4Ti_5O_{12}$ and TiO_2 react to transform the residual TiO_2 into a minor phase of $Na_2Ti_6O_{13}$; HRTEM [40] would be needed to distinguish between $Na_4Ti_5O_{12}$ and $Na_2Ti_6O_{13}$ in micrograph e. During Step 3, the two intermediate sodium titanate phases combine

Published in : Journal of Energy Chemistry (2022), vol. 65, pp. 210–218
DOI: 10.1016/j.jechem.2021.05.050
Status : Postprint (Author's version)

to form $Na_2Ti_3O_7$; the faceted rod in micrograph f can be identified as $Na_2Ti_3O_7$ based on the similarity with the SEM micrographs shown later (section 3.3). The temperature ranges indicated in Fig. 5 could represent a higher limit for the formation temperatures, since they correspond to experiments during which the temperature was increased continuously, without any hold at intermediate temperatures. Therefore, the precursor powder of spray-dried Na_2CO_3 and TiO_2 was also heat treated at 600°C, 700°C or 800°C for 8h in air. In the ex-situ diffractograms shown in Fig. 6, the mixture of $Na_4Ti_5O_{12}$ and TiO_2 observed after 8 hours at 600°C is in agreement with the scheme in Fig. 5. In the case of the treatments at 700°C and 800°C, maintaining these temperatures for 8 hours completed the reactions and led to a mixture of $Na_4Ti_5O_{12}$ and $Na_2Ti_6O_{13}$, and to $Na_2Ti_3O_7$, respectively. This was to be expected, since at these temperatures the corresponding reactions were in their initial stages in the conditions of the in-situ experiment. Obtaining $Na_2Ti_3O_7$ after 8 hours at 800°C is a much shorter duration than most of the syntheses for Na-ion battery applications starting from TiO_2 and Na_2CO_3, e.g. heat treatment of 800°C for 20h [41], 24h [33,34,42] or 40h [11,30,43–47]. By comparison, the literature data on samples prepared from a priori more homogeneous sol–gel-based precursors show that $Na_2Ti_6O_{13}$ formed between 600°C and 700°C for a heat treatment duration of 4h [14] while both Zou et al. [24] and Sauvet et al. [14] observed that $Na_2Ti_3O_7$ started to form at 700°C and that the reaction was complete at 800°C after 5h and 4h, respectively. Fig. 6 includes a diffractogram collected after a treatment of 8h at 1000°C and no evidence for $Na_2Ti_3O_7$ decomposition was found. By comparison with the sample obtained after 8h at 800°C, the cell parameters decreased by less than 0.1% and the differences in peak intensities were too small to be refined meaningfully from the laboratory XRD data. These results show that the increase in the temperature of the heat treatment could lead to small variations in the occupancy and environment of the sodium and titanium cations [48] but confirm the good structural stability at high temperatures reported in the study of Sauvet et al. [14] who observed a decomposition of the NTO material at 1100°C. However, Papp et al. [16] found indications of decomposition of $Na_2Ti_3O_7$ into $Na_2Ti_6O_{13}$ above 800°C.

3.3. PERFORMANCE AS A BATTERY ELECTRODE MATERIAL

The electrochemical performance of $Na_2Ti_3O_7$ sample obtained after 8 hours at 800°C as anode material for Na-ion batteries was evaluated. The scanning electron micrographs in Fig. 7 (a-b) show that the heat treatment at 800°C maintained the spherical shape of the spray-dried granules, with a $d_{0.5}$ value of 15.6 µm measured by laser granulometry (Fig. 7e). These spherical granules are made up of platelet- and rod-shaped primary particles of $Na_2Ti_3O_7$ with widths between 0.1 and 0.8 µm and lengths from 0.1 to 5 µm (Fig. 7c-d). The SEM cross-section in Fig. 7f shows that the entangled primary particles occupy all the sphere volume (i.e., not just the sphere crust); the EDX mapping of the sodium and titanium signals does not reveal any segregation in the cationic distribution (Fig. 7g-h). This microstructure is associated to a low BET specific surface area ($\sim 3.5 m^2/g$). Indeed, the TEM micrographs already presented in the reaction scheme of Fig. 5 showed the transition from small isotropic TiO_2 particles into larger and increasingly anisotropic particles of sodium titanate. This trend is further illustrated by the additional BET data and SEM micrographs provided in Fig. S4.

The electrochemical characterization was carried out in halfcell configuration. The voltage profiles of the charge–discharge galvanostatic cycling at C/5 are presented in Fig. 8a. Three plateaus are observed during the first discharge at C/5. In agreement with the literature [11,15,24,30,49], the plateau at about 0.5V is attributed to SEI layer formation and carbon black contribution and is associated with the ~ 60% irreversible capacity loss between the first and the second cycle. Then, Na^+ ions insert in

Published in : Journal of Energy Chemistry (2022), vol. 65, pp. 210–218
DOI: 10.1016/j.jechem.2021.05.050
Status : Postprint (Author's version)

the NTO structure in two steps at about 0.2 and 0.1V in agreement with the literature [28,49]. The following discharge curves (Fig. 8a and Fig. S5) all display only one plateau at 0.2V, as also observed by other authors. This is related to instability and changes in the structure and pathways of the NTO material during cycling [28,49,50]. The charge curves show two sodium extraction plateaus (Fig. 8a and Fig. S5): a first very short one at about 0.28 V and a second longer one at about 0.4V. After the irreversibility of the first cycle, the discharge capacity delivered in the second cycle is 137 mAh/g, i.e., 77% of the theoretical capacity. Similarly, this irreversibility leads to a very low initial coulombic efficiency during rate capability or long-term cycling tests (Fig. 8b-c). Coulombic efficiency then improves strongly during the first cycles to reach values above 98% with a slow decrease of capacity observed during long-term cycling (Fig. 8c), which is typical of the performance reported for NTO prepared by other authors [15,28,45,51–53]. When testing in cyclic voltammetry conditions at 0.1mV/s (Fig. 8d), the contribution related to carbon black and to SEI formation [28,49,51] during the first discharge is seen as a broad peak ranging from 0.23V to 0.55V. The reduction associated with sodium insertion occurs at 0.09V during the irreversible first discharge and becomes two reduction peaks at 0.16V and 0.06V during the following discharges. Sodium extraction in the charge curves appears as three peaks at 0.3V, 0.37V and 0.45V. The intensity of the peak at 0.3V falls gradually with the cycling while the peaks at 0.37V and 0.45V tend to increase. In the first report on $Na_2Ti_3O_7$ as an insertion anode for Na-ion batteries, Senguttuvan et al. [10] proposed a two-phase mechanism associated to the transition between $Na_2Ti_3O_7$ and $Na_4Ti_3O_7$. Since then, Rudola et al. [50] have observed an intermediate phase suggesting that the first discharge takes place in two steps: $Na_2Ti_3O_7 \rightarrow Na_{3-x}Ti_3O_7 \rightarrow Na_4Ti_3O_7$. Based on cycling experiments in restricted voltage ranges, Rudola et al. [50] found a lower extraction potential for $Na_{3-x}Ti_3O_7$ compared to $Na_4Ti_3O_7$. This mechanism could explain the presence of the peaks at 0.3V and 0.45V in the charge scan of the CV curves in the present work. The observed fading of the 0.3V peak and the simultaneous increase of the 0.45V peak is in agreement with the loss of the $Na_2Ti_3O_7 \rightarrow Na_{3-x}Ti_3O_7$ pathway in favour of the direct $Na_2Ti_3O_7 \rightarrow Na_4Ti_3O_7$ observed by the same authors [50].

Despite some disaggregation of the primary particles during the electrode preparation (Fig. S6), the rather large size of these primary particles explains the decrease in electrochemical performance at higher cycling rates observed in Fig. 8b. The increase in cell polarization with the cycling rate for discharge and charge processes is correlated with the decrease in the capacity (Fig. S5). Despite this, the material still delivered 110 mAh/g and 82 mAh/g at C/2 and 1C rates, respectively. The capacity recovery at C/5 after cycling at higher rates is good, confirming that this cycling rate effect is mainly kinetic.

Since XRD did not reveal alterations of the NTO structure after heat treatment at 1000°C (see Fig. 6), the electrochemical properties of this sample (Fig. S7) were was also tested. Compared to the sample prepared at 800°C, a small additional contribution related to the SEI-based irreversibility was observed at 1.1V during the first discharge [51]. The specific capacities at 1C and 2C were improved by 15% and 30%, respectively and the cycling stability at C/5 and 1C was significantly enhanced. Recently, Cao et al. [48] also reported better electrochemical performance for the NTO material prepared at 1000°C rather than at 800°C. These authors suggested that the heat treatment at 1000°C induced small structural changes compared to the structure at 800°C, leading to a more resilient NTO structure and thus facilitating the Na^+ insertion/extraction upon cycling.

Published in : Journal of Energy Chemistry (2022), vol. 65, pp. 210–218
DOI: 10.1016/j.jechem.2021.05.050
Status : Postprint (Author's version)

Fig. 9 shows that, despite the rather large particle size, the specific capacities of our material up to 1C are comparable or better than those reported in the literature for NTO prepared by solid-state reaction of TiO_2 and Na_2CO_3 [17,48,51,54–57] or NaOH [15,58]. Fig. 9 also shows that both better [24,43,59,60] and worse [7,28,49,61] performances were reported in the literature for NTO prepared by other routes (sol–gel [7,24,28,43,49,60] and hydrothermal [59,61]). Table S2 provides more detailed information about the synthesis procedures and electrochemical performance for all the literature studies included in Fig. 9.

4. CONCLUSION

When starting from a spray-dried mixture of Na_2CO_3 and TiO_2, the formation of $Na_2Ti_3O_7$ involves two intermediate sodium titanate phases, $Na_4Ti_5O_{12}$ and $Na_2Ti_6O_{13}$. For this latter phase, we observed some modifications with respect to the reference set of reflections, suggesting that although the overall framework of the structure is well-established, defects exist in the c direction. The results of the in-situ high temperature X-ray diffraction experiment are coherent with a sequence of 3 steps for the formation of $Na_2Ti_3O_7$. The equations of the chemical reactions can be qualitatively summarized by the following scenario: starting from ~ 540°C, all Na_2CO_3 reacts with part of the TiO_2 to yield $Na_4Ti_5O_{12}$; from 700°C, the remaining TiO_2 reacts with part of the $Na_4Ti_5O_{12}$ to form $Na_2Ti_6O_{13}$; finally, the two sodium titanate phases $Na_4Ti_5O_{12}$ and $Na_2Ti_6O_{13}$ react at 800°C to form $Na_2Ti_3O_7$. The formation of $Na_2Ti_3O_7$ at 800°C was completed after only 8h, compared to the usual duration of 20 to 40h for many solid-state syntheses starting from the same reagents [11,14,30,33,34,41,43–46]. When tested as an electrode material, this sample displayed the usual first cycle irreversibility due to SEI formation and carbon black contribution. The material delivered a good discharge capacity of 137 mAh/g at C/5. The decrease in the performance observed at high cycling rate was coherent with the unoptimized microstructure obtained in this study dedicated to the study of a phase formation mechanism.

Declaration of Competing Interest

The authors declare that they have no known competing financial interests or personal relationships that could have appeared to influence the work reported in this paper.

Acknowledgments

Electron microscopy (SEM and TEM) was carried out at the CAREM platform (University of Liège). The authors are grateful to the University of Liège and FRS-FNRS for equipment grants. Part of this work was supported by the Walloon Region under the ‘‘PE PlanMarshall2.vert” program (BATWAL–1318146). The authors thank Audrey Schrijnemakers and Vincent Delaval for their contribution to BET measurements and Catherine Henrist for her help for TEM microscopy.

Appendix A. Supplementary data

Supplementary data to this article can be found online at https://doi.org/10.1016/j.jechem.2021.05.050.

Published in : Journal of Energy Chemistry (2022), vol. 65, pp. 210–218
DOI: 10.1016/j.jechem.2021.05.050
Status : Postprint (Author's version)

Figures

Fig 1. *As-sprayed powder obtained by spray-drying an aqueous suspension of Na_2CO_3 and TiO_2 in stoichiometric ratio: (a) XRD pattern; (b) Thermogravimetric curve and differential scanning calorimetry curve recorded between 25°C and 900°C in air with a heating rate of 2°C/min; (c) SEM micrograph.*

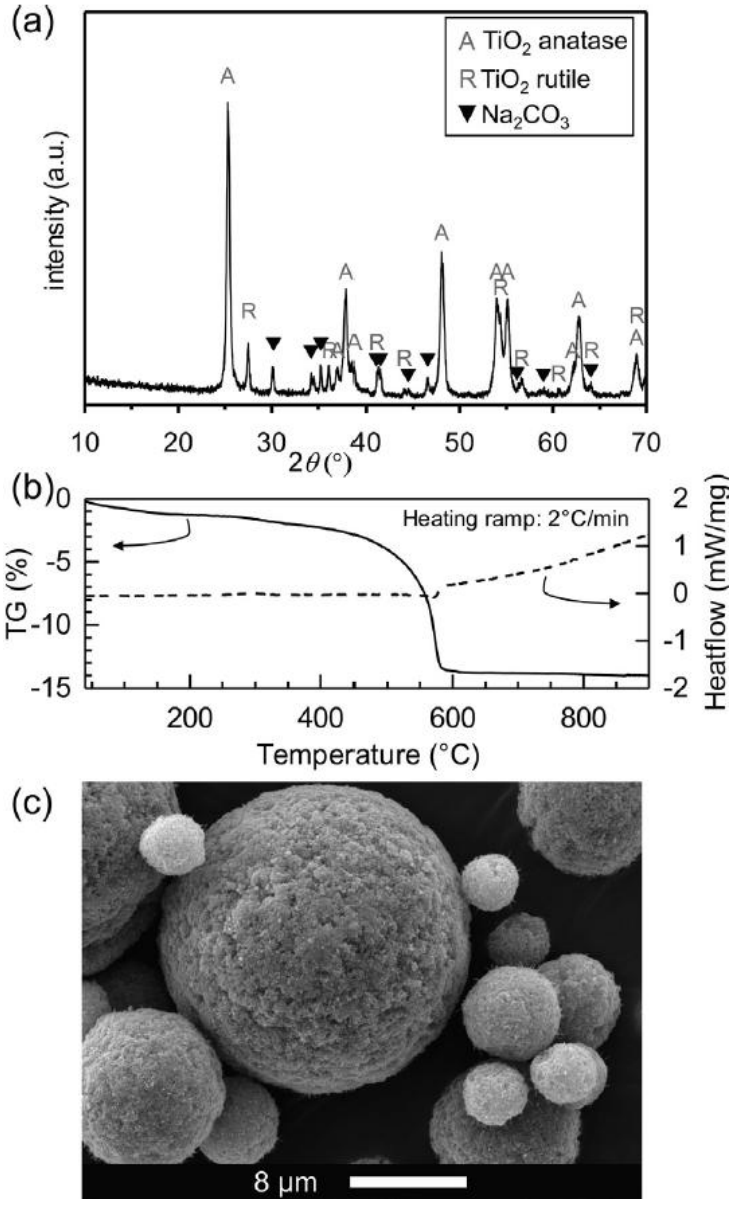

Published in : Journal of Energy Chemistry (2022), vol. 65, pp. 210–218
DOI: 10.1016/j.jechem.2021.05.050
Status : Postprint (Author's version)

***Fig 2**. In-situ high temperature X-ray diffraction of the as-sprayed powder obtained by spray-drying of a suspension of Na_2CO_3 and TiO_2 in stoichiometric ratio; 2°C/min heating in air from room temperature to 800°C, followed by a plateau at 800°C (2h). The temperature varies by 14°C during the 7min collection time of each diffractogram. Intensity maps (with higher intensity in darker grey) in the (a) 37–612°C and (b) 494–800°C ranges. The temperatures indicated on the graphs correspond to the temperature at the end of the 2θ domain. The small sharp peak at 25.5° is assigned to the Al_2O_3 signal from the crucible of the in-situ experiment. (c and d) Selected diffractograms showing the formation of new phases. The temperatures indicated on the graphs correspond to the temperature at the beginning (left) and the end (right) of the 2θ domain.*

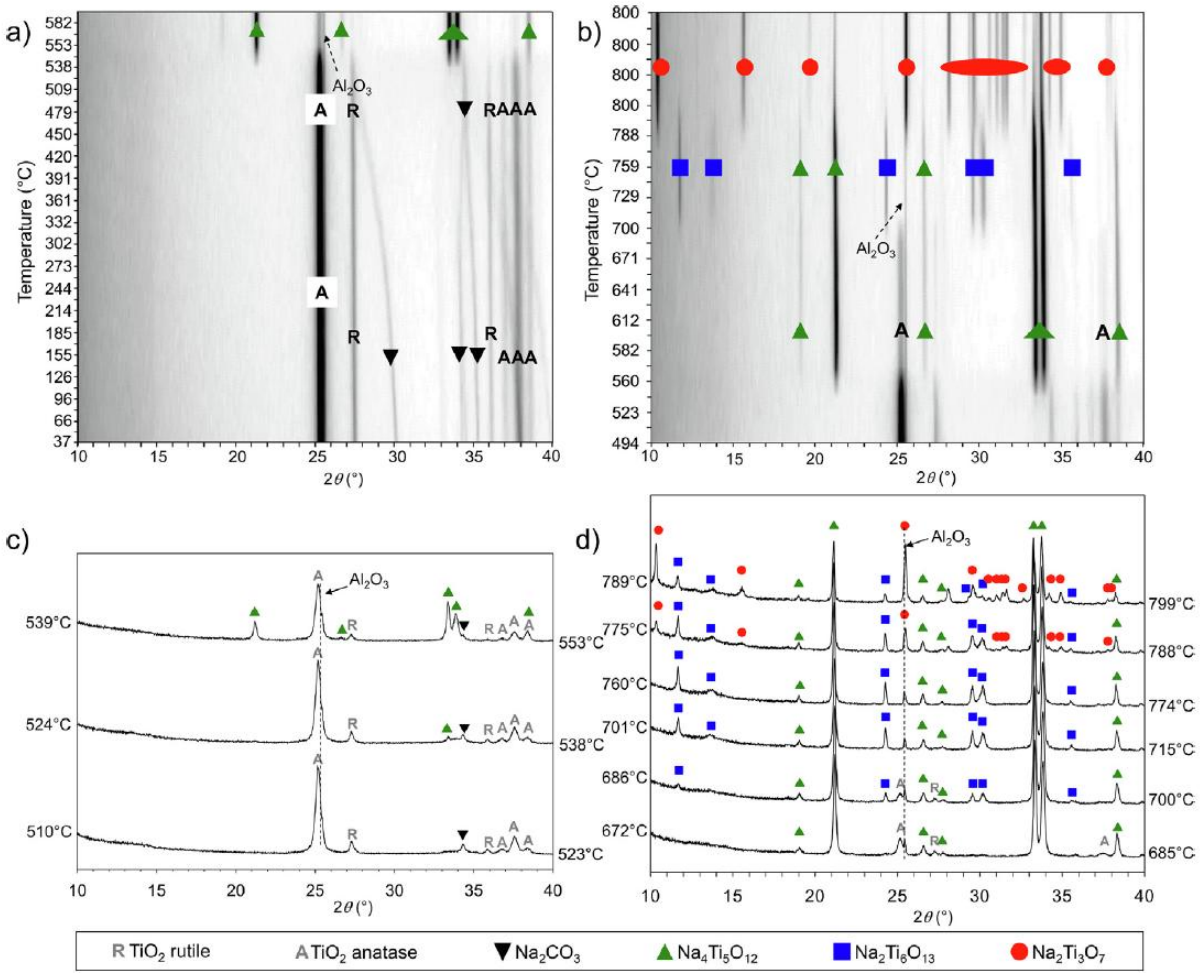

Published in : Journal of Energy Chemistry (2022), vol. 65, pp. 210–218
DOI: 10.1016/j.jechem.2021.05.050
Status : Postprint (Author's version)

Fig 3. *Temperature evolution of the peak intensities plotted from the high temperature in–situ XRD data in Fig. 2. The peak intensities correspond to the area under the peak of the following peaks: 2θ = ~25° for TiO_2 anatase, 2θ = ~21° for $Na_4Ti_5O_{12}$, 2h = ~11.5° for $Na_2Ti_6O_{13}$ and 2θ = ~10.5° for $Na_2Ti_3O_7$. The Na_2CO_3 and TiO_2 rutile signals are not shown because their intensity is too low for reliable data extraction.*

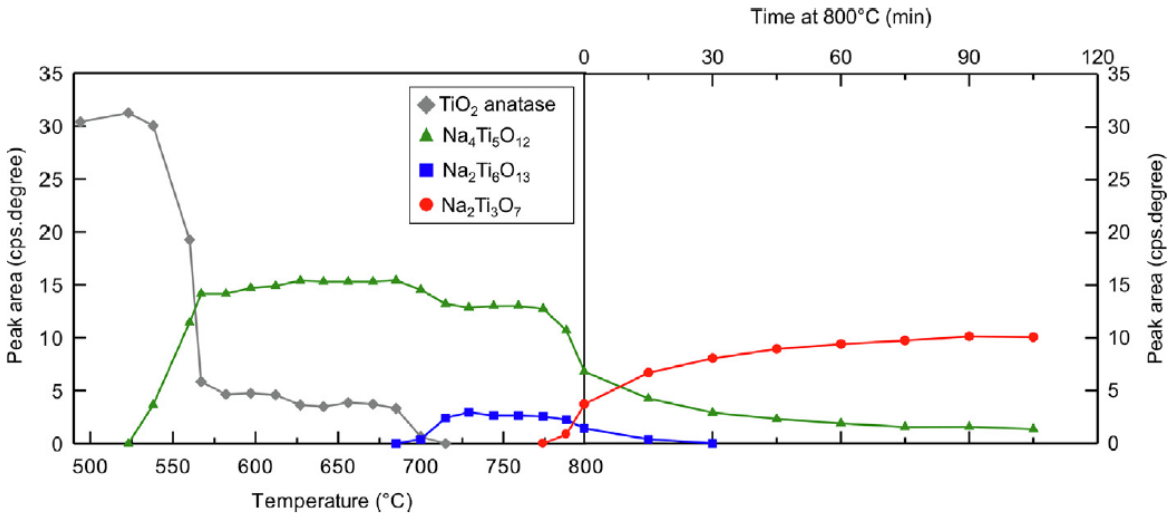

Published in : Journal of Energy Chemistry (2022), vol. 65, pp. 210–218
DOI: 10.1016/j.jechem.2021.05.050
Status : Postprint (Author's version)

Fig 4. *(a) Ex-situ X-ray diffractograms collected on samples obtained by heat treatment of spray-dried precursor powders. The sample was quenched when the furnace reached 750°C. The peak positions of the reference $Na_2Ti_6O_{13}$ phase (PDF 01-080-5525) are shown at the bottom of the graph. Green triangle symbols indicate $Na_4Ti_5O_{12}$ reflections. (b) $Na_2Ti_6O_{13}$ crystallographic structure seen along the c axis. (c) $Na_2Ti_6O_{13}$ crystallographic structure seen along the b axis.*

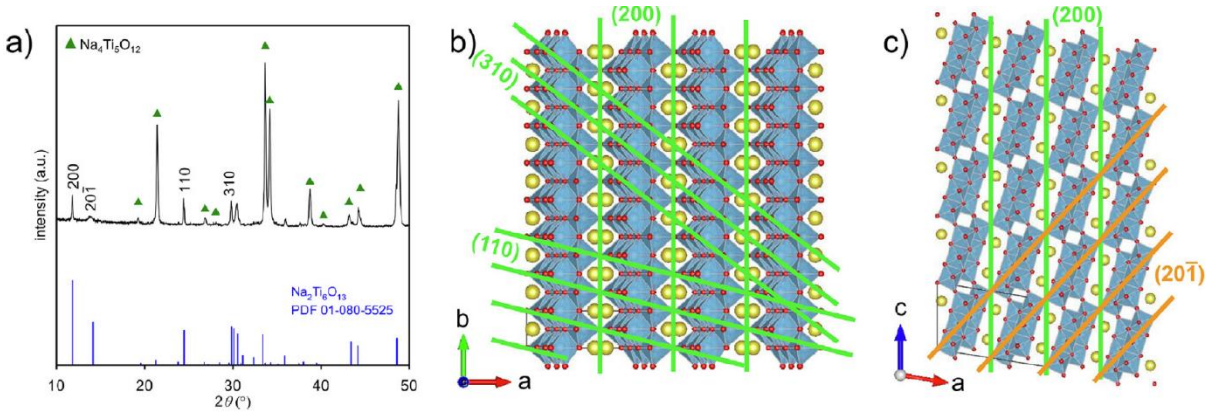

Published in : Journal of Energy Chemistry (2022), vol. 65, pp. 210–218
DOI: 10.1016/j.jechem.2021.05.050
Status : Postprint (Author's version)

Fig 5. *Overview of the formation of $Na_2Ti_3O_7$ during continuous heating at 2°C/min of a precursor powder obtained by spray-drying a suspension of Na_2CO_3 and TiO_2 in stoichiometric ratio. The colored diagram shows the evolution of the volume percentage of the different phases according to the 3 successive steps described by the chemical equations. The TEM micrographs (a-f) illustrate the evolution of the microstructure at different stages of the formation mechanism. Because of the higher thermal inertia of the larger crucible and amount of powder in the muffle furnace compared to the in-situ XRD chamber, the temperature ranges corresponding to steps 1-2-3 do not coincide exactly, as shown on the temperature axes on the left of the figure.*

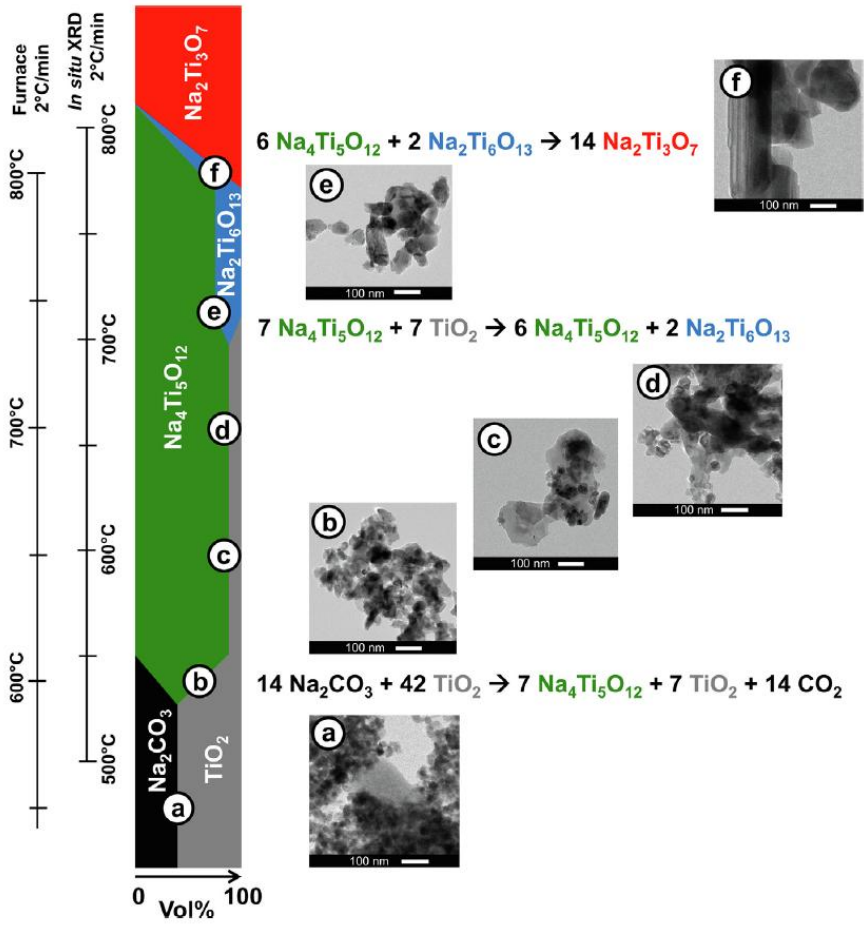

Published in : Journal of Energy Chemistry (2022), vol. 65, pp. 210–218
DOI: 10.1016/j.jechem.2021.05.050
Status : Postprint (Author's version)

Fig 6. *Ex-situ X-ray diffractograms collected on samples obtained by heat treatments of spray-dried precursor powders for 8h at different temperatures. The peak positions of the reference (PDF 00–031-1329) $Na_2Ti_3O_7$ phase are shown at the bottom of the graph for comparison with the diffractograms obtained after 8h at 800°C or 1000°C. Green triangle symbols correspond to $Na_4Ti_5O_{12}$ reflections and blue square symbols correspond to $Na_2Ti_6O_{13}$ reflections.*

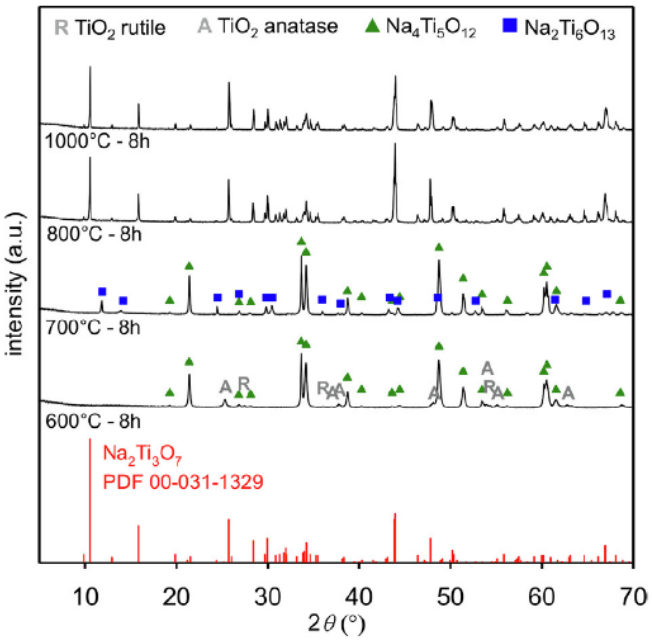

Published in : Journal of Energy Chemistry (2022), vol. 65, pp. 210–218
DOI: 10.1016/j.jechem.2021.05.050
Status : Postprint (Author's version)

Fig 7. *Powder obtained by heat treatment at 800°C for 8h of the precursors powder of spray-dried Na_2CO_3-TiO_2 in stoichiometric ratio: (a-c) SEM micrographs, (d) TEM micrograph, (e) Grain size distribution measured by laser granulometry, and (f-h) SEM cross-section and EDX mapping.*

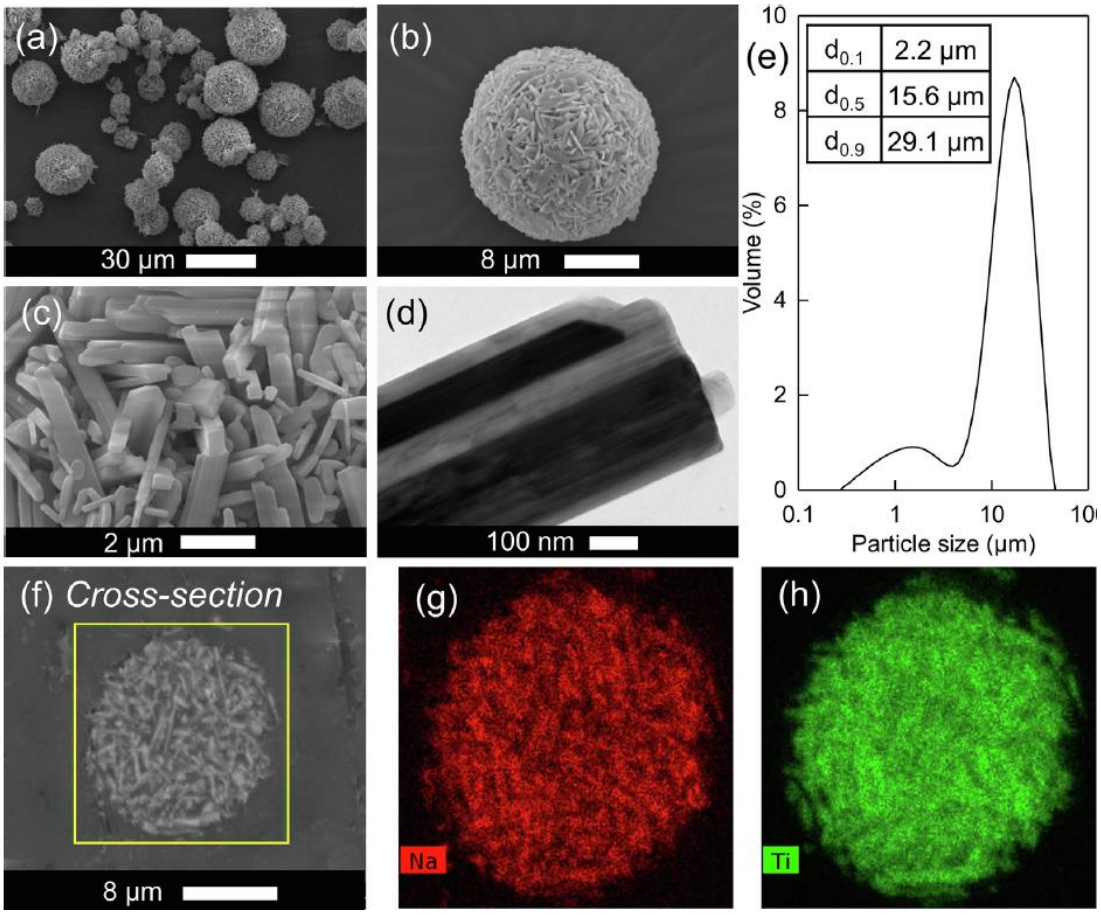

Published in : Journal of Energy Chemistry (2022), vol. 65, pp. 210–218
DOI: 10.1016/j.jechem.2021.05.050
Status : Postprint (Author's version)

Fig 8. *Electrochemical performance of $Na_2Ti_3O_7$ powder synthesized by heat treatment at 800°C for 8h of the precursor powder of spray-dried Na_2CO_3-TiO_2 in stoichiometric ratio. Mass ratios in electrode: NTO:CB:CNT:PVDF = 70:5:15:10; voltage window: 0.05–1.5V vs Na^0/Na^+, cycling rate calculated on 1C = 178 mAH/g. (a) Charge/discharge curves at C/5. (b) Specific discharge capacities and coulombic efficiency at different cycling rates. (c) Long-term cycling and coulombic efficiency at constant cycling rates rates (C/5 and 1C). (d) Cyclic voltammetry at 0.1 mV/s.*

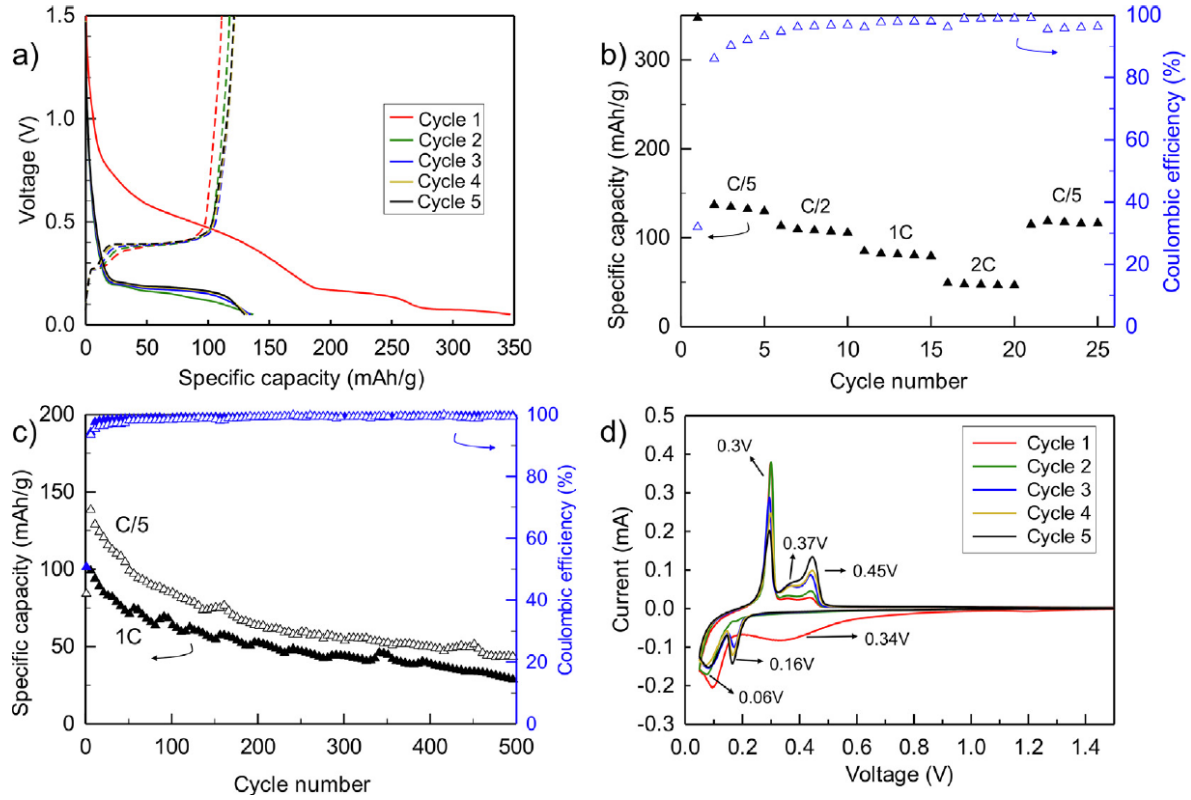

Published in : Journal of Energy Chemistry (2022), vol. 65, pp. 210–218
DOI: 10.1016/j.jechem.2021.05.050
Status : Postprint (Author's version)

Fig 9. *Comparison of the electrochemical performance of the NTO materials prepared in this work (pink and cyan marks) with literature. (a) Specific capacity vs cycling rate. (b) Specific capacity vs current density (mA/g). SS = solid state ; SG = sol–gel ; H = hydrothermal. See Table S2 for more detailed information about synthesis procedures and electrochemical performance.*

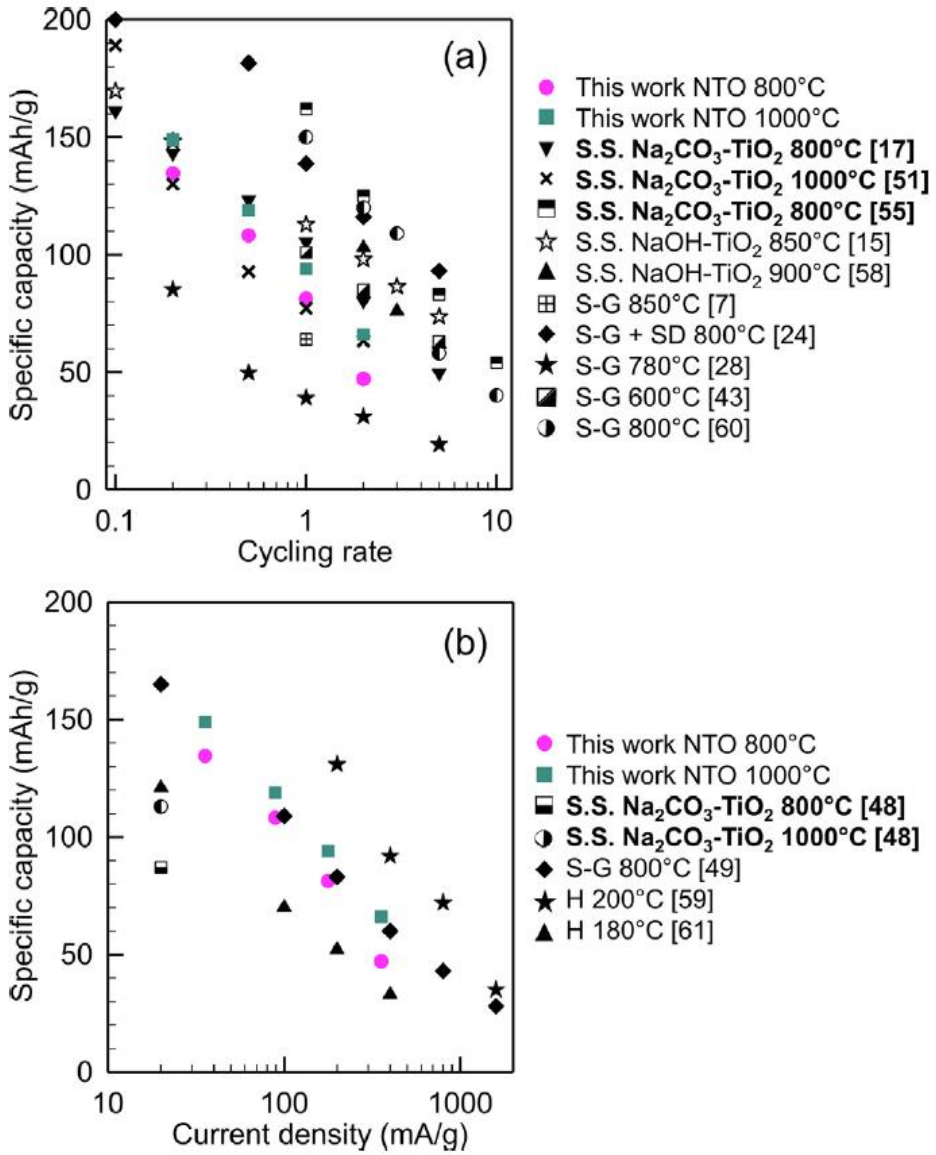

Published in : Journal of Energy Chemistry (2022), vol. 65, pp. 210–218
DOI: 10.1016/j.jechem.2021.05.050
Status : Postprint (Author's version)

References

[1] *T. Perveen, M. Siddiq, N. Shahzad, R. Ihsan, A. Ahmad, M.I. Shahzad, Renew. Sustain. Energy Rev. 119 (2020) 109549.*

[2] *F. Li, Z. Zhou, Small 14 (2018) 1–25.*

[3] *B.L. Ellis, L.F. Nazar, Curr. Opin. Solid State Mater. Sci. 16 (2012) 168–177.*

[4] *C. Nita, B. Zhang, J. Dentzer, C. Matei Ghimbeu, J. Energy Chem. 58 (2021) 207– 218.*

[5] *N. Yabuuchi, K. Kubota, M. Dahbi, S. Komaba, Chem. Rev. 114 (2014) 11636– 11682.*

[6] *I. Hasa, S. Mariyappan, D. Saurel, P. Adelhelm, A.Y. Koposov, C. Masquelier, L. Croguennec, M. Casas-Cabanas, J. Power Sources 482 (2021) 228872.*

[7] *K. Du, A. Rudola, P. Balaya, A.C.S. Appl, Mater. Interfaces 13 (2021) 11732– 11740.*

[8] *H. Zhai, B.Y. Xia, H.S. Park, J. Mater. Chem. A 7 (2019) 22163–22188.*

[9] *L.-F. Que, F.-D. Yu, L. Deng, D.-M. Gu, Z.-B. Wang, Energy Storage Mater. 25 (2020) 537–546.*

[10] *P. Senguttuvan, G. Rousse, V. Seznec, J.-M. Tarascon, M.R. Palacin, Chem. Mater. 23 (2011) 4109–4111.*

[11] *J. Nava-Avendaño, A. Morales-García, A. Ponrouch, G. Rousse, C. Frontera, P. Senguttuvan, J.-M. Tarascon, M.E. Arroyo-de Dompablo, M.R. Palacín, J. Mater. Chem. A 3 (2015) 22280–22286.*

[12] *B. Zhao, L. Lina, D. He, J. Mater. Chem. A 1 (2013) 1659–1668.*

[13] *M.J. Li, Z.Y. Chi, Y.C. Wu, J. Am. Ceram. Soc. 95 (2012) 3297–3304.*

[14] *A.-L. Sauvet, S. Baliteau, C. Lopez, P. Fabry, J. Solid State Chem. 177 (2004) 4508–4515.*

[15] *A. Rudola, K. Saravanan, C.W. Mason, P. Balaya, J. Mater. Chem. A 1 (2013) 2653–2662.*

[16] *S. Pappa, L. Korosi, V. Meynen, P. Cool, E.F. Vansant, I. Dekany, J. Solid State Chem. 178 (2005) 1614–1619.*

[17] *C.-K. Ho, C.-Y.-V. Li, K.-Y. Chan, Ind. Eng. Chem. Res. 55 (2016) 10065–10072. [18] M. Qamar, C.R. Yoon, H.J. Oh, N.H. Lee, K. Park, D.H. Kim, K.S. Lee, W.J. Lee, S.J. Kim, Catal. Today 131 (2008) 3–14.*

[18] *M. Vithal, S.R. Krishna, G. Ravi, S. Palla, R. Velchuri, S. Pola, Ceram. Int. 39 (2013) 8429–8439.*

[19] *A.B.D. Nandiyanto, K. Okuyama, Adv. Powder Technol. 22 (2011) 1–19.*

[20] *C. Piffet, B. Vertruyen, S. Caes, J. Thomassin, G. Broze, C. Malherbe, F. Boschini, R. Cloots, A. Mahmoud, Chem. Eng. J. 397 (2020) 125508.*

[21] *Y. Fang, Q. Liu, X. Feng, W. Chen, X. Ai, L. Wang, L. Wang, Z. Ma, Y. Ren, H. Yang, Y. Cao, J. Energy Chem. 54 (2021) 564–570.*

[22] *B. Vertruyen, N. Eshraghi, C. Piffet, J. Bodart, A. Mahmoud, F. Boschini, Materials (Basel). 11 (2018) 1076.*

[23] *W. Zou, J. Li, Q. Deng, J. Xue, X. Dai, A. Zhou, J. Li, Solid State Ionics 262 (2014) 192–196.*

[24] *W. Zou, Y. Wang, Z. Huang, J. Li, Sci. Sin. Chim. 44 (2014) 1347–1353.*

[25] *X. Jiang, M. Manawan, T. Feng, R. Qian, T. Zhao, G. Zhou, F. Kong, Q. Wang, S. Dai, J.H. Pan, Catal. Today 300 (2018) 12–17.*

[26] *J. Rouquerol, P. Llewellyn, F. Rouquerol, Stud. Surf. Sci. Catal. 160 (2007) 49– 56.*

[27] *H.S. Bhardwaj, T. Ramireddy, A. Pradeep, M.K. Jangid, V. Srihari, H.K. Poswal, A. Mukhopadhyay, ChemElectroChem 5 (2018) 1219–1229.*

[28] *X.-M.Z. Liudong Huang, S. woon Oh, B. Zhang, P.-C. Ma, M.M.F. Yuen, J.-K. Kim, Compos. Sci. Technol. 72 (2012) 121–144.*

[29] *M.A. Muñoz-Márquez, M. Zarrabeitia, E. Castillo-Martínez, A. Eguía-Barrio, T.*

Published in : Journal of Energy Chemistry (2022), vol. 65, pp. 210–218
DOI: 10.1016/j.jechem.2021.05.050
Status : Postprint (Author's version)

[30] *Rojo, M. Casas-Cabanas, A.C.S. Appl, Mater. Interfaces 7 (2015) 7801–7808.*
[31] *P. Ballirano, Phase Transitions 84 (2011) 357–379.*
[32] *I.A. Stenina, L.D. Kozina, T.L. Kulova, A.M. Skundin, Russ. J. Inorg. Chem. 61 (2016) 1235–1240.*
[33] *M. Zarrabeitia, E. Castillo-Martínez, J.M. Lopez Del Amo, A. Eguía-Barrio, M.A. Munoz-Marquez, T. Rojo, M. Casas-Cabanas, Acta Mater. 104 (2016) 125–130. [34] M. Zarrabeitia, F. Nobili, M.A. Munoz-Marquez, T. Rojo, M. Casas-Cabanas, J. Power Sources 330 (2016) 78–83.*
[34] *K. Kataoka, J. Awaka, N. Kijima, H. Hayakawa, K.I. Ohshima, J. Akimoto, Chem. Mater. 23 (2011) 2344–2352.*
[35] *P. Li, P. Wang, S. Qian, H. Yu, X. Lin, M. Shui, X. Zheng, N. Long, J. Shu, Electrochim. Acta 187 (2016) 46–54.*
[36] *J.C. Pérez-Flores, F. García-Alvarado, M. Hoelzel, I. Sobrados, J. Sanzc, A. Kuhn, Dalt. Trans. 41 (2012) 14633–14642.*
[37] *S. Andersson, A.D. Wadsley, Acta Crystallogr. 15 (1962) 194–201.*
[38] *L.M. Torres-Martínez, I. Juárez-Ramírez, K. Del Ángel-Sánchez, L. Garza-Tovar, A. Cruz-López, G. Del Ángel, J. Sol-Gel Sci. Technol. 47 (2008) 158–164.*
[39] *C. Wu, W. Hua, Z. Zhang, B. Zhong, Z. Yang, G. Feng, W. Xiang, Z. Wu, X. Guo, Adv. Sci. 5 (2018).*
[40] *A.A. Araújo-filho, F.L.R. Silva, A. Righi, B. Mauricélio, P. Silva, E.W.S. Caetano, V. N. Freire, J. Solid State Chem. 250 (2017) 68–74.*
[41] *M. Zarrabeitia, E. Castillo-Martínez, J.M. López Del Amo, A. Eguía-Barrio, M.A. Muñoz-Márquez, T. Rojo, M. Casas-Cabanas, J. Power Sources 324 (2016) 378– 387.*
[42] *M. Zukalová, B.P. Lásková, K. Mocek, A. Zukal, M. Bouša, L. Kavan, J. Solid State Electrochem. 22 (2018) 2545–2552.*
[43] *G. Rousse, M.E.A. Dompablo, P. Senguttuvan, A. Ponrouch, J.-M. Tarascon, M.R. Palacín, Chem. Mater. 25 (2013) 4946–4956.*
[44] *J. Xu, C. Ma, M. Balasubramanian, Y. Shirley, Chem. Commun. 50 (2014) 12564–12567.*
[45] *M. Dynarowska, J. Kotwi, M. Leszczynska, M. Marzantowicz, F. Krok, Solid State Ionics 301 (2017) 35–42.*
[46] *T.K. Saothayanun, T.T. Sirinakorn, M. Ogawa, Inorg. Chem. 59 (2020) 4024– 4029.*
[47] *Y. Cao, Q. Ye, F. Wang, X. Fan, L. Hu, F. Wang, T. Zhai, H. Li, Adv. Funct. Mater. 30 (2020) 2003733.*
[48] *T.L.Y.O.A.A. KulovaKudryashovaKuz'mina, I.A. Stenina, A.A. Chekannikov, A.B.*
[49] *Yaroslavtsev, J. Libich, J. Solid State Electrochem. 23 (2019) 455–463.*
[50] *A. Rudola, N. Sharma, P. Balaya, Electrochem. Commun. 61 (2015) 10–13.*
[51] *H. Pan, L. Xia, X. Yu, Y.-S. Hu, H. Li, X.-Q. Yang, L. Chen, Adv. Energy Mater. 3 (2013) 1186–1194.*
[52] *W. Wang, C. Yu, Z. Lin, J. Hou, H. Zhua, S. Jiao, Nanoscale 5 (2013) 594–599.*
[53] *C. Ding, T. Nohira, R. Hagiwara, J. Power Sources 354 (2017) 10–15.*
[54] *M. Youssry, A. Mussa, Ceram. Int. 47 (2021) 14021–14032.*
[55] *S.I.R. Costa, Y.S. Choi, A.J. Fielding, A.J. Naylor, J.M. Griffin, Z. Sofer, D.O. Scanlon, N. Tapia-Ruiz, Chem. - A Eur. J. 27 (2021) 3875–3886.*
[56] *S. Chauque, F.Y. Oliva, G. Lener, O.R. Cámara, J. Solid State Electrochem. 24 (2020) 1017–1032.*
[57] *S. Altin, S. Demirel, E. Oz, E. Altin, C. Hetherington, A. Bayri, S. Avci, CrystEngComm 22 (2020) 2483–2490.*
[58] *J. Xia, H. Zhao, W.K. Pang, Z. Yin, B. Zhou, G. He, Z. Guo, Y. Du, Chem. Sci. 9 (2018) 3421–3425.*
[59] *S. Chen, L. Gao, L. Zhang, X. Yang, Ionics (Kiel). 25 (2019) 2211–2219.*
[60] *T. Song, S. Ye, H. Liu, Y.G. Wang, J. Alloys Compd. 767 (2018) 820–828.*

Published in : Journal of Energy Chemistry (2022), vol. 65, pp. 210–218
DOI: 10.1016/j.jechem.2021.05.050
Status : Postprint (Author's version)

[61] *Z. Chen, Q. Zhang, L. Lu, X. Chen, S. Wang, C. Xin, B. Xing, C. Zhang, Energy Fuels 34 (2020) 3901–3908.*